Draft version August 12, 2022
Typeset using LaTeX twocolumn style in AASTeX631

Updated High-Temperature Opacities for The Dartmouth Stellar Evolution Program and their Effect on the Jao Gap Location

Thomas M. Boudreaux[1] and Brian C. Chaboyer[1]

[1] *Department of Physics and Astronomy, Dartmouth College, Hanover, NH 03755, USA*

ABSTRACT

The Jao Gap, a 17 percent decrease in stellar density at $M_G \sim 10$ identified in both Gaia DR2 and EDR3 data, presents a new method to probe the interior structure of stars near the fully convective transition mass. The Gap is believed to originate from convective kissing instability wherein asymmetric production of ^{3}He causes the core convective zone of a star to periodically expand and contract and consequently the stars' luminosity to vary. Modeling of the Gap has revealed a sensitivity in its magnitude to a population's metallicity primarily through opacity. Thus far, models of the Jao Gap have relied on OPAL high-temperature radiative opacities. Here we present updated synthetic population models tracing the Gap location modeled with the Dartmouth stellar evolution code using the OPLIB high-temperature radiative opacities. Use of these updated opacities changes the predicted location of the Jao Gap by $\sim$0.05 mag as compared to models which use the OPAL opacities.

Keywords: Stellar Evolution (1599) — Stellar Evolutionary Models (2046)

1. INTRODUCTION

Due to the initial mass requirements of the molecular clouds which collapse to form stars, star formation is strongly biased towards lower mass, later spectral class stars when compared to higher mass stars. Partly as a result of this bias and partly as a result of their extremely long main-sequence lifetimes, M Dwarfs make up approximately 70 percent of all stars in the galaxy. Moreover, some planet search campaigns have focused on M Dwarfs due to the relative ease of detecting small planets in their habitable zones (e.g. Nutzman & Charbonneau 2008). M Dwarfs then represent both a key component of the galactic stellar population as well as the possible set of stars which may host habitable exoplanets. Given this key location M Dwarfs occupy in modern astronomy it is important to have a thorough understanding of their structure and evolution.

Jao et al. (2018) discovered a novel feature in the Gaia Data Release 2 (DR2) $G_{BP} - G_{RP}$ color-magnitude-diagram. Around $M_G = 10$ there is an approximately 17 percent decrease in stellar density of the sample of stars Jao et al. (2018) considered. Subsequently, this has become known as either the Jao Gap, or Gaia M Dwarf Gap. Following the initial detection of the Gap in DR2 the Gap has also potentially been observed in 2MASS (Skrutskie et al. 2006; Jao et al. 2018); however, the significance of this detection is quite weak and it relies on the prior of the Gap's location from Gaia data. Further, the Gap is also present in Gaia Early Data Release 3 (EDR3) (Jao & Feiden 2021). These EDR3 and 2MASS data sets then indicate that this feature is not a bias inherent to DR2.

The Gap is generally attributed to convective instabilities in the cores of stars straddling the fully convective transition mass (0.3 - 0.35 $M_\odot$) (Baraffe & Chabrier 2018). These instabilities interrupt the normal, slow, main sequence luminosity evolution of a star and result in luminosities lower than expected from the main sequence mass-luminosity relation (Jao & Feiden 2020).

The Jao Gap, inherently a feature of M Dwarf populations, provides an enticing and unique view into the interior physics of these stars (Feiden et al. 2021). This is especially important as, unlike more massive stars, M Dwarf seismology is infeasible due to the short periods and extremely small magnitudes which both radial and low-order low-degree non-radial seismic waves are predicted to have in such low mass stars (Rodríguez-López 2019). The Jao Gap therefore provides one of the

Corresponding author: Thomas M. Boudreaux
thomas.m.boudreaux.gr@dartmouth.edu,
thomas@boudreauxmail.com

only current methods to probe the interior physics of M Dwarfs.

Despite the early success of modeling the Gap some issues remain. Jao & Feiden (2020, 2021) identify that the Gap has a wedge shape which has not been successful reproduced by any current modeling efforts and which implies a somewhat unusual population composition of young, metal-poor stars. Further, Jao & Feiden (2020) identify substructure, an additional over density of stars, directly below the Gap, again a feature not yet fully captured by current models.

All currently published models of the Jao Gap make use of OPAL high temperature radiative opacities. Here we investigate the effect of using the more up-to-date OPLIB high temperature radiative opacities and whether these opacity tables bring models more in line with observations. In Section 2 we provide an overview of the physics believed to result in the Jao Gap, in Section 3 we review the differences between OPAL and OPLIB and describe how we update DSEP to use OPLIB opacity tables. In Section 4 we validate the update opacities by generating solar calibrated stellar models. Section 5 walks through the stellar evolution and population synthesis modeling we perform. Finally, in Section 6 we present our findings.

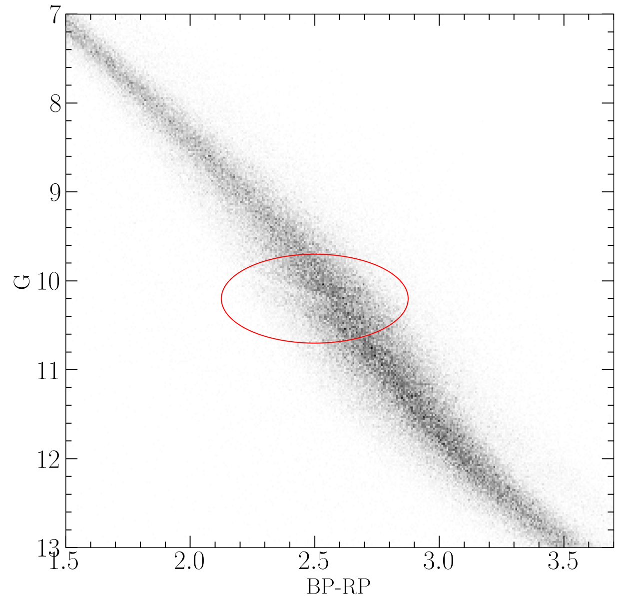

Figure 1. The Jao Gap seen in the Gaia Catalogue of Nearby Stars (circled)

2. JAO GAP

A theoretical explanation for the Jao Gap (Figure 1) comes from van Saders & Pinsonneault (2012), who propose that in a star directly above the transition mass, due to asymmetric production and destruction of ^{3}He during the proton-proton I chain (ppI), periodic luminosity variations can be induced. This process is known as convective-kissing instability. Such a star will descend the pre-main sequence with a radiative core; however, as the star reaches the zero age main sequence (ZAMS) and as the core temperature exceeds 7×10^6 K, enough energy will be produced by the ppI chain that the core becomes convective. At this point the star exists with both a convective core and envelope, in addition to a thin, radiative layer separating the two. Subsequently, asymmetries in ppI affect the evolution of the star's convective core.

The proton-proton I chain constitutes three reactions

1. $p + p \longrightarrow d + e^+ + \nu_e$
2. $p + d \longrightarrow \ ^3\mathrm{He} + \gamma$
3. $^3\mathrm{He} +^3 \mathrm{He} \longrightarrow \ ^3\mathrm{He} + 2p$

Because reaction 3 of ppI consumes ^{3}He at a slower rate than it is produced by reaction 2, core ^{3}He abundance, and consequently the rate of reaction 3, increases with time. The core convective zone expands as more of the star becomes unstable to convection. This expansion continues until the core connects with the convective envelope. At this point convective mixing can transport material throughout the entire star and the high concentration of ^{3}He rapidly diffuses outward, away from the core, decreasing energy generation as reaction 3 slows down. Ultimately, this leads to the convective region around the core pulling back away from the convective envelope, leaving in place the radiative transition zone, at which point ^{3}He concentrations grow in the core until it once again expands to meet the envelope. These periodic mixing events will continue until ^{3}He concentrations throughout the star reach an equilibrium ultimately resulting in a fully convective star. Figure 2 traces the evolution of a characteristic star within the Jao Gap's mass range.

2.1. *Efforts to Model the Gap*

Since the identification of the Gap, stellar modeling has been conducted to better constrain its location, effects, and exact cause. Both Mansfield & Kroupa (2021) and Feiden et al. (2021) identify that the Gap's mass location is correlated with model metallicity — the mass-luminosity discontinuity in lower metallicity models being at a commensurately lower mass. Feiden et al. (2021) suggests this dependence is due to the steep relation of the radiative temperature gradient, ∇_{rad}, on temperature and, in turn, on stellar mass.

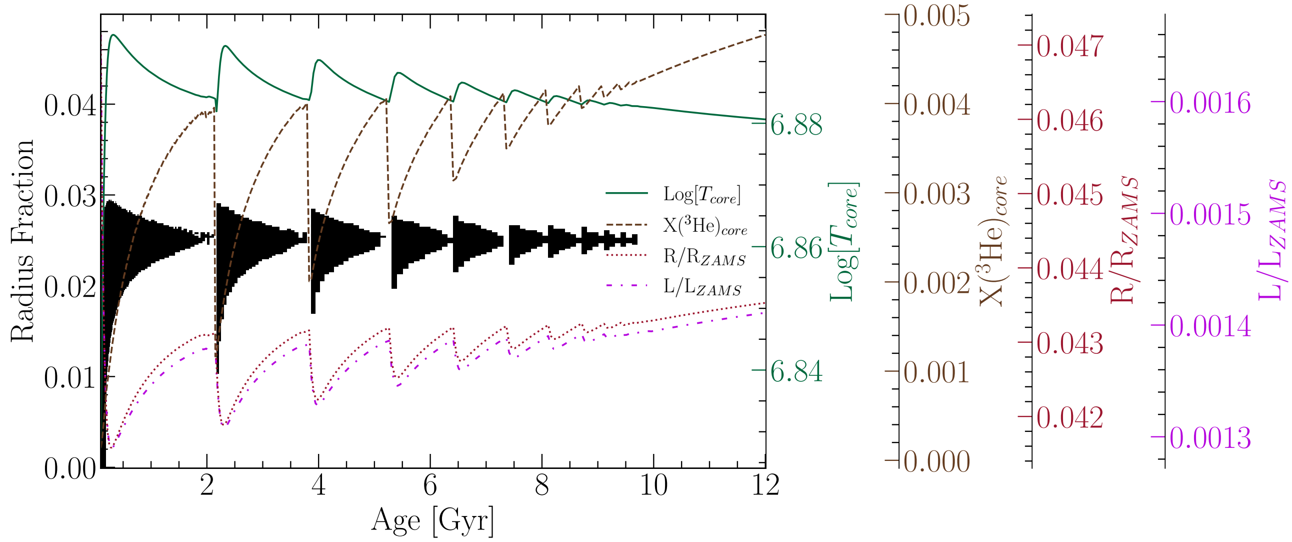

Figure 2. Kippenhan diagram for a characteristic stellar model of 0.35625 $M_{\odot}$ which is within the Jao Gap's mass range. The black shaded regions denote whether, at a particular model age, a radial shell within the model is radiative or convective (with white meaning convective and black meaning radiative). The lines trace the models core temperature, core ^{3}He mass fraction, fractional luminosity wrt. the zero age main sequence and fractional radius wrt. the zero age main sequence.

$$\nabla_{rad} \propto \frac{L\kappa}{T^4} \tag{1}$$

As metallicity decreases so does opacity, which, by Equation 1, dramatically lowers the temperature at which radiation will dominate energy transport (Chabrier & Baraffe 1997). Since main sequence stars are virialized the core temperature is proportional to the core density and total mass (Equation 2). Therefore, if the core temperature where convective-kissing instability is expected decreases with metallicity, so too will the mass of stars which experience such instabilities.

$$T_c \propto \rho_c M^2 \tag{2}$$

The strong opacity dependence of the Jao Gap begs the question: **what is the effect of different opacity [estimates?] on Gap properties**. As we can see above, changing opacity should affect the Gap's location in the mass-luminosity relation and therefore in a color-magnitude diagram. Moreover, current models of the Gap have yet to locate it precisely in the CMD (Feiden et al. 2021) with an approximate 0.16 G-magnitude difference between the observed and modeled Gaps. Opacity provides one, as yet unexplored, knob to turn which has the potential to resolve these discrepancies.

3. UPDATED OPACITIES

Multiple groups have released high-temperature opacities including, the Opacity Project (OP Seaton et al. 1994), Laurence Livermore National Labs OPAL opacity tables (Iglesias & Rogers 1996), and Los Alamos National Labs OPLIB opacity tables (Colgan et al. 2016). OPAL high-temperature radiative opacity tables in particular are very widely used by current generation isochrone grids (e.g. Dartmouth, MIST, & StarEvol, Dotter et al. 2008; Choi et al. 2016; Amard et al. 2019). However, they are relatively old and therefore do not incorporate the most up-to-date understanding of plasma modeling in their code (Colgan et al. 2016)

While the overall effect on the CMD of using OPLIB compared to OPAL tables is small, the strong theoretical opacity dependence of the Jao Gap raises the potential for these small effects to measurably shift the Gap's location. We update DSEP to use high temperature opacity tables based on measurements from Los Alamos national Labs T-1 group (OPLIB, Colgan et al. 2016). The OPLIB tables use the ATOMIC. ATOMIC (Magee et al. 2004; Hakel et al. 2006; Fontes et al. 2015) is a modern LTE and non-LTE opacity and plasma modeling code which was used to generate opacity tables in an attempt to resolve the discrepancy between helioseismic and solar model predictions of chemical abundances in the sun (Bahcall et al. 2005). For a detailed breakdown of how the most up-to-date set of OPLIB tables are generated see (Colgan et al. 2013a,b, 2015, 2016).

OPLIB tables include monochromatic Rosseland mean opacities — composed from bound-bound, bound-free, free-free, and scattering opacities — for elements hydrogen through zinc over temperatures 0.5eV to 100 keV and for mass densities from approximately 10^{-8} g

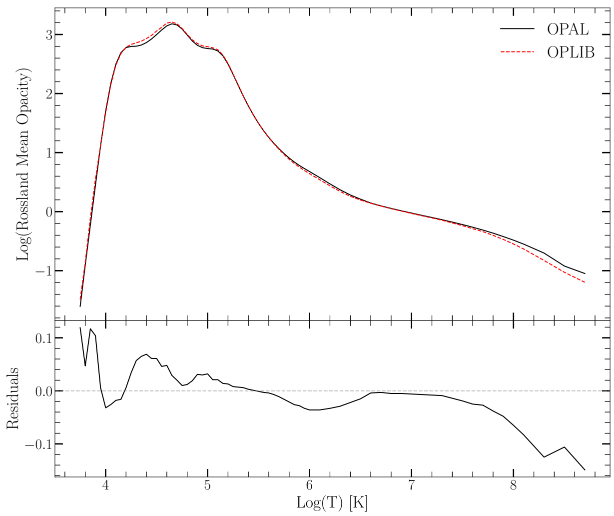

Figure 3. Rosseland mean opacity with the GS98 solar composition for both OPAL opacities and OPLIB opacities (top). Residuals between OPLIB opacities and OPAL opacities (bottom). These opacities are plotted at $\log_{10}(R) = -1.5$, $X = 0.7$, and $Z = 0.02$. Note how the OPLIB opacities are systematically lower than the OPAL opacities for temperatures above 10^6 K.

cm^{-3} up to approximately 10^4 g cm^{-3} (though the exact mass density range varies as a function of temperature).

When comparing OPAL and OPLIB opacity tables (Figure 3) we find OPLIB opacities are systematically lower than OPAL opacities for temperatures above 10^6 K. These lower opacities will decrease the radiative temperature gradient. Consequently, the radiative layer in a stellar model evolved using OPLIB opacity tables should be closer into the model core than it would be in models making use of OPAL tables.

3.1. *Table Querying and Conversion*

The high-temperature opacity tables used by DSEP give Rosseland-mean opacity, κ_R, along three dimensions: temperature, a density proxy R, and composition. R is defined as

$$R = \frac{\rho}{T_6^3} \tag{3}$$

Where $T_6 = T \times 10^{-6}$ and ρ is the mass density. If T and ρ are given in cgs then for much of the radius of a star $\log(R) \sim -1.5$ [CITATION]. R is used, as opposed to simply tracking opacity over mass density, because of its small dynamic range when compared to ρ ($\rho \sim 10^5$ [g cm^{-3}] at the core of an RGB star all the way down to $\sim 10^{-8}$ [g cm^{-3}] within the envelope).

OPLIB tables are queried from a web interface[1]. In order to generate many tables easily and quickly we develop a web scraper built with Python's `requests` module in addition to the 3rd party `mechanize` and `BeautifulSoup` modules (Chandra & Varanasi 2015; Richardson 2007) which can automatically retrieve all the tables needed to build an opacity table that DSEP can make use of. This web scraper submits a user requested chemical composition (composed of mass fractions for elements from hydrogen to zinc) to the Los Alamos web form, selects 0.0005 keV as the lower temperature bound and 60 keV as the upper temperature bound, and finally requests opacity measurements for 100 densities, ranging from $1.77827941 \times 10^{-15}$ [g cm^{-3}] up to 1×10^7 [g cm^{-3}], at each temperature interval. These correspond to approximately the same temperature and density range of opacities present in the OPAL opacity tables. For a detailed discussion of how OPLIB tables are transformed into a format DSEP can use see Appendix A.

4. SOLAR CALIBRATED STELLAR MODELS

In order to validate the OPLIB opacities, we generate a solar calibrated stellar model (SCSM) using these new tables. We allow both the convective mixing length parameter, α_{ML}, and the initial Hydrogen mass fraction, X, to vary simultaneously, minimizing the difference between resultant models' final radius and luminosity to those of the sun.

Optimization of α_{ML} and X is conducted using gradient descent. For each optimization step three models are evolved: a reference model, a model with a small perturbation to the hydrogen mass fraction but the same mixing length as the reference model, and a model with a small perturbation to the mixing length but the same hydrogen mass fraction as the reference. Perturbations are sampled from a normal distribution (using `numpy.random`). This distribution is sampled and that sample is then added to the reference value for either X or α_{ML}. The luminosity and radius of the three evolved models are compared to solar values and the gradient of the resultant $L - L_\odot$, $R - R_\odot$ surface is followed down to new estimates for the reference values of X and α_{ML}. This process is is repeated until the difference between successive X and α_{ML} drops below one part in 10^5.

Solar calibrated stellar models evolved using GS98 OPAL and OPLIB opacity tables (Figure 4) differ $\sim$ 0.5% in the SCSM hydrogen mass fractions and $\sim 1.5\%$

[1] https://aphysics2.lanl.gov/apps/

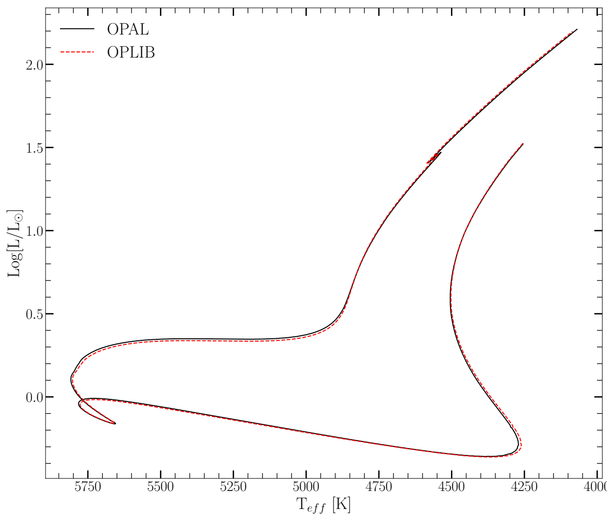

Figure 4. HR Diagram for the two SCSMs, OPAL and OPLIB. OPLIB is shown as a grey dashed line.

Model	X	α_{ML}
OPAL	0.7066	1.9333
OPLIB	0.7107	1.9629

Table 1. Optimized parameters for SCSMs evolved using OPAL and OPLIB high temperature opacity tables.

in the SCSM convective mixing length parameters (Table 1). While the two evolutionary tracks are very similar, note that the OPLIB SCSM's luminosity is systematically lower at the same age until the star leaves the main sequence, at which point it is effectively the same as the OPAL SCSM. This luminosity difference between OPAL and OPLIB based models is consistent with expectations given the shallow radiative temperature gradient resulting from the lower OPLIB opacities

5. MODELING

In order to model the Jao Gap we evolve two extremely finely sampled mass grids of models. One of these grids uses the OPAL high-temperature opacity tables while the other uses the OPLIB tables (Figure 5). Each grid evolves a model every 0.00025 $M_\odot$ from 0.2 to 0.4 $M_\odot$ and every 0.005 $M_\odot$ from 0.4 to 0.8 $M_\odot$. All models in both grids use a GS98 solar composition, the (1, 101, 0) `Free_EOS` (version 2.7) configuration, and 1000 year old pre-main sequence polytropic models, with polytropic index 1.5, as their initial conditions.

Because in this work we are just interested in the location shift of the Gap as the opacity source varies, we do not model variations in composition. Mansfield & Kroupa (2021); Jao & Feiden (2020); Feiden et al. (2021) all look at the effect composition has on Jao Gap location. They find that as population metallicity increases so too does the mass range and consequently the magnitude of the Gap. From an extremely low metallicity population (Z=0.001) to a population with a more solar like metallicity this shift in mass range can be up to 0.05 M$_\odot$ (Mansfield & Kroupa 2021).

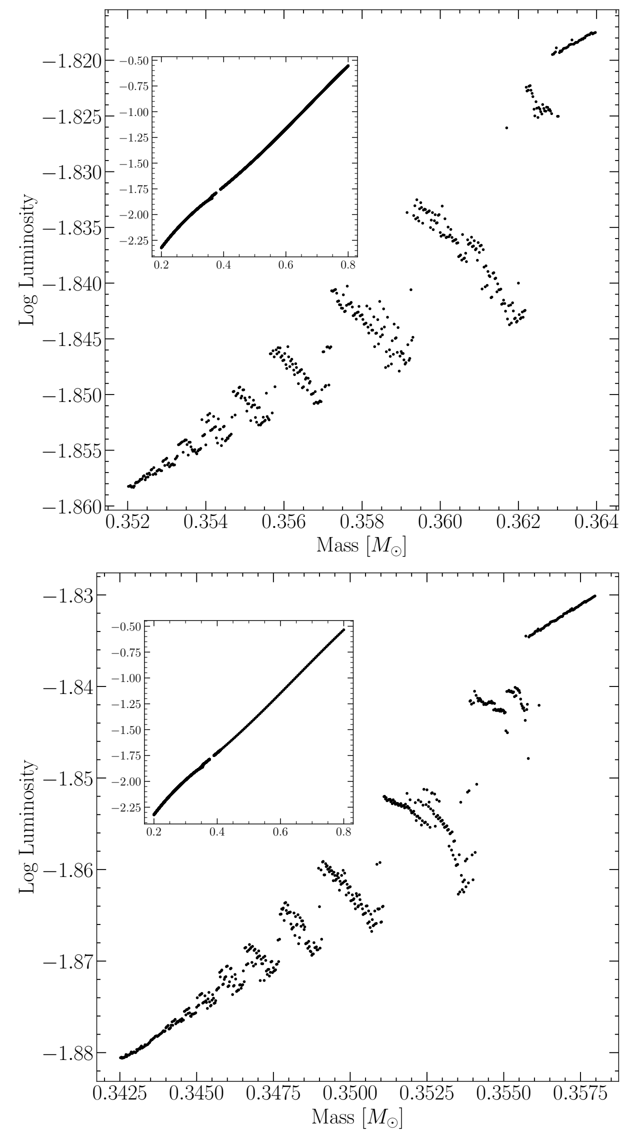

Figure 5. Mass-luminosity relation for models evolved using OPAL opacity tables (top) and those evolved using OPLIB opacity tables (bottom) [UPDATE OPLIB FIG WHEN MODELS DONE]. Note the lower mass range of the OPLIB Gap.

5.1. *Population Synthethis*

In order to compare the Gap to observations we use in house population synthesis code. Our population synthesis code first uses inverse CDF sampling to build a distribution of target masses from some initial

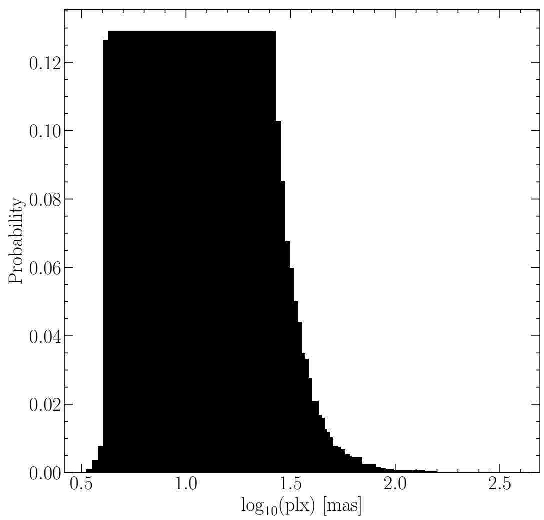

Figure 6. Probability distribution sampled when assigning true parallaxes to synthetic stars. This distribution is built from the GCNS.

mass function (IMF). Specifically we use the Sollima (2019) IMF where, for masses $0.25\ M_{\odot} < M < 1M_{\odot}$, $\alpha = -1.34 \pm 0.07$. The model nearest in mass to the samples mass above and the nearest model below are then selected from the evolved model database. The surface gravity, luminosity, and effective temperature of the sample are estimated from a linear interpolation between the upper and lower bounding models. T_{eff}, g, and $\log(L)$ are transformed to Gaia G, BP, and RP magnitudes using the Gaia (E)DR3 bolometric corrections (Creevey et al. 2022) along with code obtained thorough personal communication with Aaron Dotter [How to cite Aaron's color code?]. Next, we introduce observationally informed photometric and astrometric uncertainties into our population.

We select the Gaia Catalogue of Nearby Stars (GCNS) (Gaia Collaboration et al. 2021) to empirically calibrate uncertainty relations. A function with the form of Equation 4 is fit to parallax uncertainty vs. G magnitude. Additionally, a function of the form of Equation 5 is fit to to i$^{\text{th}}$ (G, BP, RP) magnitude uncertainty vs. i$^{\text{th}}$ magnitude.

$$\sigma_{plx}(M_g) = ae^{bM_g} + c \tag{4}$$

$$\sigma_i(M_i) = ae^{M_i - b} + c \tag{5}$$

Each of these functions estimates the uncertainty of some quantity at a given magnitude. Moreover, for each sampled star in the synthetic population we select a parallax from the distribution in the GCNS (Figure 6), referred to as the "true parallax". A parallax uncertainty is calculated based on the empirically calibrated parallax uncertainty and G-magnitude relation along with the synthetic stars G-magnitude (hereafter the "true" G magnitude) and the results of the fitting described in the previous paragraph. This uncertainty is then, with equal weighting, either added or subtracted from the true parallax, yielding an "observed parallax".

The true parallax is used to convert the true i$^{\text{th}}$ magnitude to an apparent i$^{\text{th}}$ magnitude and the observed parallax is used to convert the apparent i$^{\text{th}}$ magnitude into an observed i$^{\text{th}}$ magnitude. Finally, each observed magnitude is summed with an estimated photometric uncertainty for that magnitude based on the fit of the i$^{\text{th}}$ magnitude to the uncertainty in the i$^{\text{th}}$ magnitude.

To summarize the process that each synthetic star will go through

1. Sample from a Sollima (2019) IMF to determine synthetic star mass.
2. Find the closest model above and below the synthetic star, lineally interpolate model parameters to the synthetic star mass.
3. Convert synthetic star g, T_{eff}, and $Log(L)$ to Gaia G, BP, and RP colors.
4. Sample from the GCNS to assign synthetic star a "true" parallax.
5. Evaluate the empirical calibration given in Equation 4 to find an associated parallax uncertainty and adjust the true parallax by this value resulting in an observed parallax.
6. Use the true parallax to find an apparent magnitude for each filter.
7. Use the observed parallax and the apparent magnitude to find an observed magnitude.
8. Evaluate the empirical calibration given in Equation 5 to give a magnitude uncertainty scale in each band.
9. Adjust each magnitude by some amount sampled from a normal distribution with a standard deviation of the magnitude uncertainty scale.

This method then incorporates both photometric and astrometric uncertainties into our population synthesis. An example 7 Gyr old synthetic populations using OPAL and OPLIB opacities are presented in Figure 7.

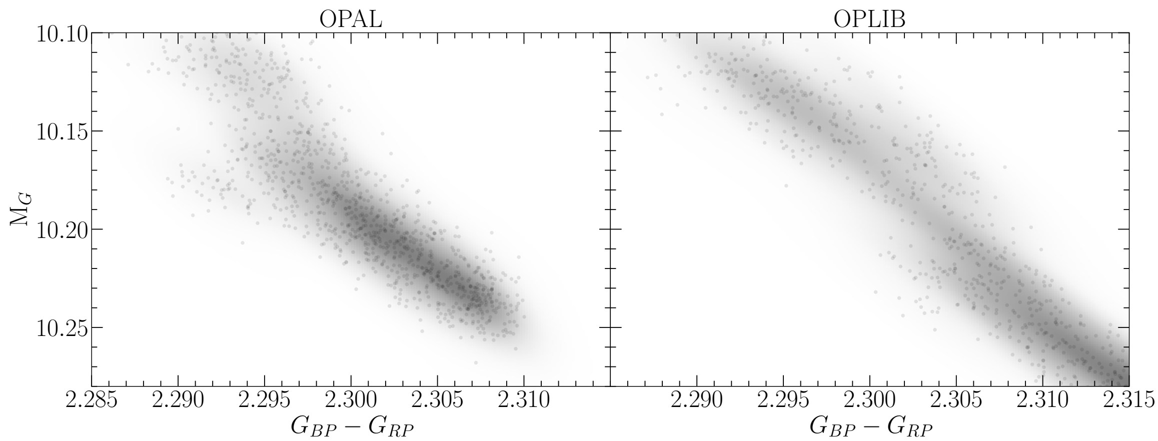

Figure 7. Population synthesis results for models evolved with OPAL (left) and models evolved with OPLIB (right). A Gaussian kernel-density estimate has been overlaid to better highlight the density variations. [THIS IS A PLACEHOLDER FIGURE]

Model	Location	Prominence
OPAL	10.15864	0.19501
OPLIB 1	10.17813	0.26055
OPLIB 2	10.21313	0.46898

Table 2. Locations identified as potential Gaps.

6. RESULTS

We quantify the Jao Gap location along the magnitude axis by sub-sampling our synthetic populations, finding the linear number density along the magnitude axis of each sub-sample, averaging these linear number densities, and extracting any peaks above some prominence threshold. Once we have the peak location we fit a Gaussian to a window centered at the peak giving both an estimate of the Gap location and the Gap width. Figure 8 shows this fit for both OPAL and OPLIB populations.

Our Gap identification method finds two potential Gaps in the OPLIB (Table 2) data while only finding one in the OPAL dataset. This apparent discrepancy is not due to a fundamental structural difference between the OPAL and OPLIB opacity tables; rather, it is attributable to the phasing of the periodic luminosity variations seen across mass in Figure 5 and whether or not the injected noise smears all of these together into one Gap or two Gaps.

[There will be text detailing a test where I manually shift the OPAL data to the same phase as the OPLIB in an attempt to explain the extra Gap seen in OPLIB].

Both Gaps identified in the OPLIB sample are at fainter magnitudes than the Gap identified in the OPAL sample. Consequently, in the OPLIB sample the convective mixing events which drive the kissing instability happen more regularly and therefore also start earlier in the model's evolution. This is because each mixing event serves to interrupt the "standard" luminosity evolution of a stellar model, kicking its luminosity back down to what it would have been at some earlier stage of stellar evolution instead of allowing it to slowly increase.

Convective mixing events starting earlier in a model's evolution are consistent with the slightly lower opacities characteristic to OPLIB. A lower opacity fluid will have a more shallow radiative temperature gradient than a higher opacity fluid; however, as the adiabatic temperature gradient remains essentially unchanged as a function of radius, a larger interior radius of the model will remain unstable to convection [CHECK IF THIS OR IF RADIATIVE ZONE MOVING IN]. This larger convective zone, and therefore smaller radiative zone, is in line with the behavior of the models presented here as it with the radiative zone closer to the convective zone it takes less time for that radiative zone to heat up and become unstable to convection. We see that OPLIB models undergo convective mixing events earlier in their evolution than OPAL models (Figure 9) implying that the inner convective zone did not have to expand as much to meet the outer convective zone.

The most precise published Gap location comes from Jao & Feiden (2020) who use EDR3 to locate the Gap at $M_G \sim 10.3$, we identify the Gap at a similar location in the GCNS data. **The Gap in populations evolved using OPLIB tables is closer to this measurement than it is in populations evolved using OPAL tables (Table 2).** It should be noted that the exact location of the observed Gap is poorly captured by a single value as the Gap visibly compresses across the width of the main-sequence, wider on the blue edge and narrower on the red edge such that the observed Gap has downward facing a wedge shape (Figure 1). This wedge

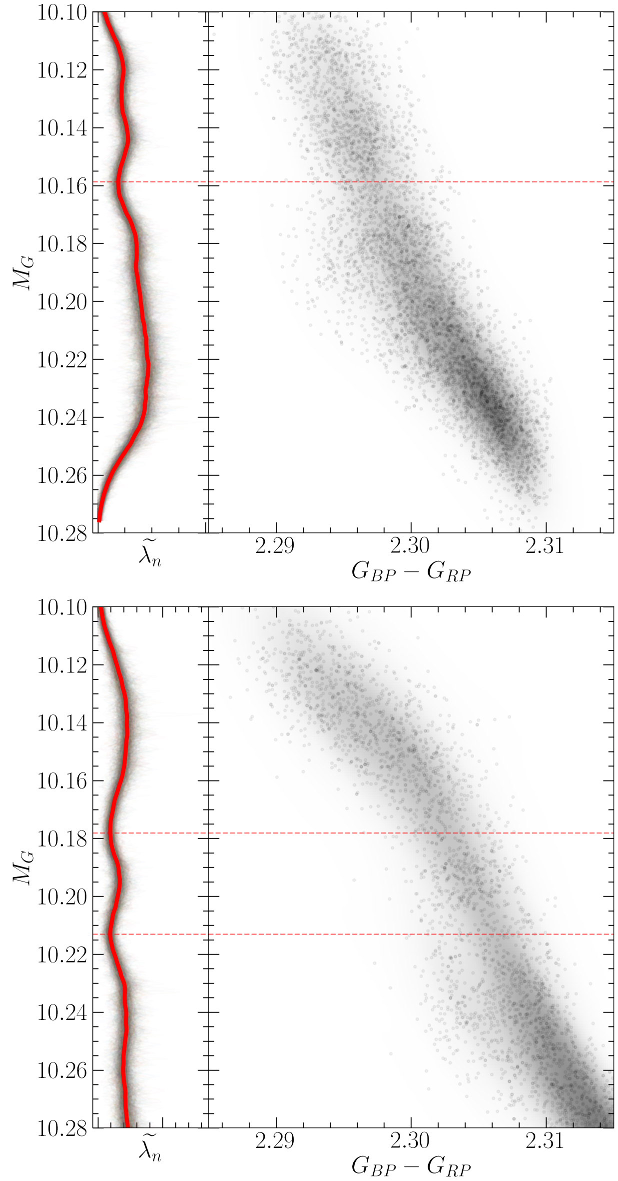

Figure 8. (right panels) OPAL (top) and OPLIB (bottom) synthetic populations. (left panels) Normalized linear number density along the magnitude axis. A dashed line has been extended from the peak through both panels to make clear where the identified Jao Gap location is wrt. to the population.

shape is not successfully reproduced by either any current models or the modeling we preform here. We elect then to specify the Gap location where this wedge is at its narrowest, on the red edge of the main sequence.

The Gaps identified in our modeling have widths of approximately 0.03 magnitudes, while the shift from OPAL to OPLIB opacities is anywhere from 0.02 to 0.05 magnitudes. With the prior that the Gaps clearly shift before noise is injected we know that this shift is real. How-

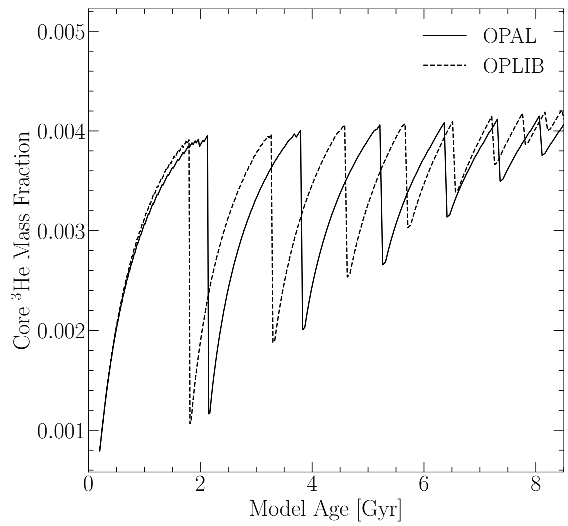

Figure 9. Core ^{3}He mass fraction for a model evolved with OPAL and a model evolved with OPLIB within the Jao Gap's mass range. Note how the OPLIB model undergoes the mixing event earlier in its evolution than the OPAL model does.

ever, since the shift magnitude and Gap width are of approximately the same size in our synthetic populations its likely that in a real population — with both compositional and age variations which we do not account for — **the Gap location will not provide a usable constraint on the opacity source.**

7. CONCLUSION

The Jao Gap provides an intriguing probe into the interior physics of M Dwarfs stars where traditional methods of studying interiors break down. However, before detailed physics may be inferred it is essential to have models which are well matched to observations. Here we investigate whether the OPLIB opacity tables reproduce the Jao Gap location and structure more accurately than the widely used OPAL opacity tables. We find that while the OPLIB tables do shift the Jao Gap location more in line with observations the shift is small enough that it is likely not distinguishable from noise due to population age and chemical variation. Moreover, we do not find that the OPLIB opacity tables help in reproducing the wedge shape of the observed Gap.

APPENDIX

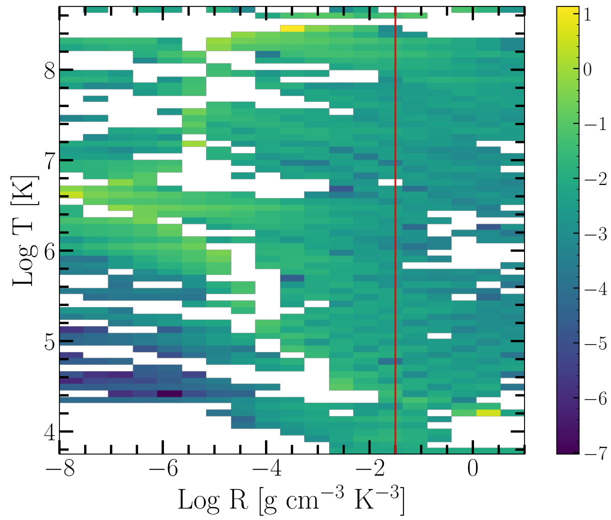

Figure 10. Log Fractional Difference between opacities in $\kappa_R(\rho, T_{eff})$ space directly queried from the OPLIB web-form and those which have been interpolated into $\log(R)$ space and back. Note that, due to the temperature grid DSEP uses not aligning perfectly which the temperature grid OPLIB uses there may be edge effects where the interpolation is poorly constrained. The red line corresponds to $\log(R) = -1.5$ where much of a stellar model's radius exists.

A. INTERPOLATING $\rho \rightarrow$ R

OPLIB reports κ_R as a function of mass density, temperature in keV, and composition. DSEP uses tables where opacity is given as a function of temperature in Kelvin, R, and composition. The conversion from temperature in keV to Kelvin is trivial

$$T_K = T_{keV} * 11604525.0061657 \tag{A1}$$

However, the conversion from mass density to R is more involved. Because R is coupled with both mass density and temperature there there is no way to directly convert tabulated values of opacity reported in the OPLIB tables to their equivalents in R space. Instead we must rotate the tables, interpolating $\kappa_R(\rho, T_{eff}) \rightarrow \kappa_R(R, T_{eff})$.

To preform this rotation we use the `interp2d` function within `scipy`'s `interpolate` (Virtanen et al. 2020) module to construct a cubic bivariate B-spline (Dierckx 1981) interpolating function s, with a smoothing factor of 0, representing the surface $\kappa_R(\rho, T_{eff})$. For each R^i and T^j_{eff} which DSEP expects high-temperature opacities to be reported for, we evaluate Equation 3 to find $\rho^{ij} = \rho(T^j_{eff}, R^i)$. Opacities in T_{eff}, R space are then inferred as $\kappa^{ij}_R(R^i, T^j_{eff}) = s(\rho^{ij}, T^j_{eff})$.

As first-order validation of this interpolation scheme we can preform a similar interpolation in the opposite direction, rotating the tables back to $\kappa_R(\rho, T_{eff})$ and then comparing the initial, "raw", opacities to those which have gone through the interpolations process. Figure 10 shows the fractional difference between the raw opacities and a set which have gone through this double interpolation. The red line denotes $\log(R) = -1.5$ where models will tend to sit for much of their radius. Along the $\log(R) = -1.5$ line the mean fractional difference is $\langle\delta\rangle = 0.006$ with an uncertainty of $\sigma_{\langle\delta\rangle} = 0.009$. One point of note is that, because the initial rotation into $\log(R)$ space also reduces the domain of the opacity function interpolation-edge effects which we avoid initially by extending the domain past what DSEP needs cannot be avoided when interpolating back into ρ space.

This work has made use of the NASA astrophysical data system (ADS). We would like to thank Elisabeth Newton, Aaron Dotter, and Gregory Feiden for their support and for useful disscusion related to the topic of this paper. Additionally, we would like to thank James Colgan for his assistance with the OPLIB opacity tables. We acknowledge the support of a NASA grant (No. 80NSSC18K0634).

Software: The Dartmouth Stellar Evolution Program (Dotter et al. 2008), BeautifulSoup (Richardson 2007), mechanize (Chandra & Varanasi 2015)

REFERENCES

Amard, L., Palacios, A., Charbonnel, C., et al. 2019, A&A, 631, A77, doi: 10.1051/0004-6361/201935160

Bahcall, J. N., Serenelli, A. M., & Basu, S. 2005, ApJL, 621, L85, doi: 10.1086/428929

Baraffe, I., & Chabrier, G. 2018, A&A, 619, A177, doi: 10.1051/0004-6361/201834062

Chabrier, G., & Baraffe, I. 1997, A&A, 327, 1039. https://arxiv.org/abs/astro-ph/9704118

Chandra, R. V., & Varanasi, B. S. 2015, Python requests essentials (Packt Publishing Ltd)

Choi, J., Dotter, A., Conroy, C., et al. 2016, ApJ, 823, 102, doi: 10.3847/0004-637X/823/2/102

Colgan, J., Kilcrease, D. P., Magee, N. H., et al. 2015, High Energy Density Physics, 14, 33, doi: 10.1016/j.hedp.2015.02.006

—. 2013a, High Energy Density Physics, 9, 369, doi: 10.1016/j.hedp.2013.03.001

Colgan, J., Kilcrease, D. P., Magee, N. H., J., et al. 2013b, in American Institute of Physics Conference Series, Vol. 1545, Eighth International Conference on Atomic and Molecular Data and Their Applications: ICAMDATA-2012, ed. J. D. Gillaspy, W. L. Wiese, & Y. A. Podpaly, 17–26

Colgan, J., Kilcrease, D. P., Magee, N. H., et al. 2016, in APS Meeting Abstracts, Vol. 2016, APS Division of Atomic, Molecular and Optical Physics Meeting Abstracts, D1.008

Creevey, O. L., Sordo, R., Pailler, F., et al. 2022, arXiv e-prints, arXiv:2206.05864. https://arxiv.org/abs/2206.05864

Dierckx, P. 1981, IMA Journal of Numerical Analysis, 1, 267, doi: 10.1093/imanum/1.3.267

Dotter, A., Chaboyer, B., Jevremović, D., et al. 2008, The Astrophysical Journal Supplement Series, 178, 89

Feiden, G. A., Skidmore, K., & Jao, W.-C. 2021, ApJ, 907, 53, doi: 10.3847/1538-4357/abcc03

Fontes, C. J., Zhang, H. L., Abdallah, J., J., et al. 2015, Journal of Physics B Atomic Molecular Physics, 48, 144014, doi: 10.1088/0953-4075/48/14/144014

Gaia Collaboration, Smart, R. L., Sarro, L. M., et al. 2021, A&A, 649, A6, doi: 10.1051/0004-6361/202039498

Hakel, P., Sherrill, M. E., Mazevet, S., et al. 2006, JQSRT, 99, 265, doi: 10.1016/j.jqsrt.2005.04.007

Iglesias, C. A., & Rogers, F. J. 1996, ApJ, 464, 943, doi: 10.1086/177381

Jao, W.-C., & Feiden, G. A. 2020, AJ, 160, 102, doi: 10.3847/1538-3881/aba192

—. 2021, Research Notes of the American Astronomical Society, 5, 124, doi: 10.3847/2515-5172/ac053a

Jao, W.-C., Henry, T. J., Gies, D. R., & Hambly, N. C. 2018, ApJL, 861, L11, doi: 10.3847/2041-8213/aacdf6

Magee, N. H., Abdallah, J., Colgan, J., et al. 2004, in American Institute of Physics Conference Series, Vol. 730, Atomic Processes in Plasmas: 14th APS Topical Conference on Atomic Processes in Plasmas, ed. J. S. Cohen, D. P. Kilcrease, & S. Mazavet, 168–179

Mansfield, S., & Kroupa, P. 2021, A&A, 650, A184, doi: 10.1051/0004-6361/202140536

Nutzman, P., & Charbonneau, D. 2008, PASP, 120, 317, doi: 10.1086/533420

Richardson, L. 2007, April

Rodríguez-López, C. 2019, Frontiers in Astronomy and Space Sciences, 6, 76, doi: 10.3389/fspas.2019.00076

Seaton, M. J., Yan, Y., Mihalas, D., & Pradhan, A. K. 1994, MNRAS, 266, 805, doi: 10.1093/mnras/266.4.805

Skrutskie, M. F., Cutri, R. M., Stiening, R., et al. 2006, AJ, 131, 1163, doi: 10.1086/498708

Sollima, A. 2019, Monthly Notices of the Royal Astronomical Society, 489, 2377, doi: 10.1093/mnras/stz2093

van Saders, J. L., & Pinsonneault, M. H. 2012, ApJ, 751, 98, doi: 10.1088/0004-637X/751/2/98

Virtanen, P., Gommers, R., Oliphant, T. E., et al. 2020, Nature Methods, 17, 261, doi: 10.1038/s41592-019-0686-2